PCCP

PAPER

View Article Online
View Journal | View Issue

Check for updates

Cite this: *Phys. Chem. Chem. Phys.*, 2020, **22**, 4549

Catalytic performance of Pd_n (n = 1, 2, 3, 4 and 6) clusters supported on TiO_{2-V} for the formation of dimethyl oxalate *via* the CO catalytic coupling reaction: a theoretical study†

Lixia Ling,*[ab] Yueting Cao,[a] Min Han,[a] Ping Liu,[b] Riguang Zhang[c] and Baojun Wang *[c]

Received 17th December 2019,
Accepted 24th January 2020

DOI: 10.1039/c9cp06773f

rsc.li/pccp

The formation of dimethyl oxalate (DMO) *via* CO catalytic coupling on a series of catalysts including Pd_n (n = 1, 2, 3, 4 and 6) clusters loaded on TiO_{2-V} has been explored by density functional theory (DFT) calculation. The results show that different Pd_n clusters have a remarkable influence on DMO formation. The Pd_1/TiO_{2-V} catalyst is not suitable for the CO catalytic coupling reaction since CO is easily bound to the O atom on the surface of TiO_{2-V} leading to the formation of CO_2. The activity of four catalysts complies with the following order of Pd_4/TiO_{2-V} > Pd_6/TiO_{2-V} > Pd_2/TiO_{2-V} > Pd_3/TiO_{2-V} by comparing the activation energy barriers of the rate-determining steps in the optimal paths. Charge analysis implies that less charge is transferred from the Pd_4/TiO_{2-V} and Pd_6/TiO_{2-V} catalysts to CO than on the other catalysts, which leads to the relatively weak adsorption of CO, and therefore CO has a greater tendency to react with other species on the surface. In addition, Pd_6/TiO_{2-V} also exhibits relatively higher selectivity toward DMO than the other three catalysts. Therefore, Pd_6 is regarded as a suitable cluster, which is supported on TiO_{2-V} demonstrating high catalytic activity and selectivity to DMO.

Introduction

CO catalytic coupling to dimethyl oxalate (DMO) is a pivotal step in coal-to-ethylene glycol (CTEG) processes, during which the conversion of inorganic C1 to organic C2 is realized.[1] Metal palladium (Pd) as a catalyst has been used in many important organic reactions.[2] Recently, Pd-based nanomaterial catalysts have been found to have wide utilization in heterogeneous catalytic processes, and what's more, rich experimental and theoretical studies on the synthesis process of DMO *via* CO catalytic coupling over Pd-based catalysts have been done.[2–6] However, high cost and scarce reserves of Pd bulk on the earth make its application in industry more difficult.[3,5] In view of the present situation, it is necessary to seek a Pd-based catalyst with high economic benefits and catalytic performance for the formation of DMO. It is well known that both the geometrical structures of the Pd surface and Pd size have an influence on catalytic performance. Pd clusters exhibit many different properties from those of micro and macro substances. In addition, Pd clusters contain different atomic numbers with different physicochemical properties.[7,8]

Usually, metal particles exhibit special characteristics compared with the surface, and therefore they have received extensive attention and have been applied to various aspects.[9–16] Moreover, it has been shown that different sizes of Pd clusters display various catalytic activities aiming at the same reaction.[17–19] In general, the potential activities of catalysts in clusters are distinctly attributed to the smaller average coordination number in small particles than in large crystals.[12–21] It was proved that ultra-small copper clusters exhibited remarkable catalytic activity compared with the larger size catalysts for the formation of methanol.[9] The reaction mechanisms of $2CO + 2NO \rightarrow N_2 + 2CO_2$ on Pd clusters with various sizes are distinctly different.[22] It was also proved that an Au single atom supported on suitable oxide supports is extremely activated for CO oxidation *via* both experimental and theoretical studies.[23] Recent research by Tahereh *et al.* found that Pd_2 could be used as a favorable catalyst for the selective hydrogenation of acetylene in comparison to the Pd_{12} nanocluster.[24] In general, compared to bulk alloys, small metal particles have unique properties and specific interactions with supports, so small cluster supported catalysts have unique properties.[25] The adsorptions of

[a] College of Chemistry and Chemical Engineering, Taiyuan University of Technology, Taiyuan 030024, P. R. China. E-mail: linglixia@tyut.edu.cn
[b] State Key Laboratory of Coal Conversion, Institute of Coal Chemistry, Chinese Academy of Sciences, Taiyuan 030001, P. R. China
[c] Key Laboratory of Coal Science and Technology of Ministry of Education and Shanxi Province, Taiyuan University of Technology, Taiyuan 030024, P. R. China. E-mail: wangbaojun@tyut.edu.cn

† Electronic supplementary information (ESI) available. See DOI: 10.1039/c9cp06773f

C_2H_4 on isolated Pd_4, Pd_4/γ-$A1_2O_3(100)$ and Pd_4/γ-$A1_2O_3(110)$ were studied, and this showed that C_2H_4 adsorption in π mode is favorable on isolated Pd_4 and Pd_4/γ-$A1_2O_3(110)$, whereas the di-σ mode is preferred on Pd_4/γ-$A1_2O_3(100)$.[25] Ultra-dispersed Pd clusters supported on alumina also showed higher activity for CO oxidation than Pd(111).[26] The catalytic reduction of NO by C_3H_8 was studied over zeolite supported small Pd clusters, and the results showed that it displayed a prominent catalytic activity, and N_2 is the only reduced product in the temperature range of 573–873 K.[27,28] The BN-supported sub-nanometer Pd_6 cluster for the decomposition of HCOOH was studied, and HCOO-mediated and COOH-mediated paths were considered. It was found that the former path is more favorable on the Pd_6 cluster than the latter one, and the under-coordinated metal atoms in the sub-nanometer cluster played an important role.[29] In addition, adsorption energies of H on Pd_n (n = 3, 4 and 5) clusters supported on graphene are greater than that on the Pd(111) surface by density functional theory (DFT) calculation.[30] And the Pd_n ($n \leq 6$) cluster loaded on the alumina support is generally more reactive than the larger clusters for CO oxidation.[31] All the above studies show that metal clusters have great application prospects in catalytic reactions due to their special structures.

Titanium dioxide is a promising heterogeneous catalyst with good photoelectric and photochemical properties. It has been the preferred system for industrial application for many years, and has been widely used in many fields of materials and catalysts.[32–34] Due to the unique physical properties of crystal phases in titanium dioxide, it can be divided into three main types: anatase, rutile and brookite.[35,36] Anatase titania is thought to be more active compared with the rutile phase.[37] According to the research of Li *et al.*,[35] there was a strong metal-support interaction (SMSI) effect between Pd metal and an anatase titania catalyst at a low-temperature while for rutile there is not. This is mainly due to the existence of Ti^{3+}, which was obtained by the reduction of Ti^{4+}.[38] By the study of Sanz and Márquez,[39] DFT calculation indicated that Pd atoms had stronger binding ability with the O-vacancy surface than that with the perfect surface. According to the research of Yang *et al.*,[38] it was found that significant charge transfer resulted from the existence of O-vacancies, which led to a strong ability to capture the Pd_4 cluster on the O-vacancy surface, and the same result was also obtained by previous studies.[40,41] In addition, the periodic DFT study also showed that the step-by-step hydrogenation of ethylene on the surface of $Co_3O_4(111)$ with O-vacancies was easier than that on the perfect surface.[42]

Previous studies have shown that the (001) facet of titania is considerably more active than the (101) one.[43,44] In this work, different Pd clusters with different structures supported on $TiO_2(001)$ with an O-vacancy are discussed in order to find which Pd metal size is more suitable for the formation of DMO. The single atom catalyst is first considered due to its special catalytic property and high atomic efficiency.[45] Pd_2 and Pd_3 are different two-dimensional structures, Pd_2 is linear[46] and Pd_3 is the smallest planar structure,[47] and they are often chosen to investigate the adsorption of CO. The most stable Pd_4 and Pd_6 clusters are small and three-dimensional structures, and were proved to be the stable magic number clusters in our previous work[48] and other works.[49,50] As compared with the Pd_4 and Pd_6 clusters, the relative stability of the Pd_5 cluster is lower. Therefore, Pd_5 is not considered in this work. A suitable catalyst with less precious metal Pd, high activity and DMO selectivity will be screened out at last.

Calculation details

Calculation methods

A periodic plane-wave DFT+U study was performed in the Vienna ab initio simulation package (VASP).[51,52] The generalized gradient approximation (GGA) is implemented in the exchange–correlation functional of Perdew–Burke–Ernzerhof (PBE).[53] A plane wave with a cut-off energy of 400 eV (1 eV = 96.485 kJ mol^{-1}) was used. The k-point was sampled at a density of $6 \times 6 \times 6$ for the bulk of TiO_2, and a k-point of $2 \times 2 \times 1$ for the $p(3 \times 3)$ supercell was used. The U value of Ti was determined as 4 eV[39] to evaluate the on-site coulomb interactions in the localized d orbital and exchange interactions. The Gaussian smearing method was employed to improve the convergence of states near the Fermi level with the value of SIGMA = 0.2 eV. All geometries were optimized until the force and energy on each atom were converged to 0.03 eV $Å^{-1}$ and 1×10^{-5} eV, respectively. Moreover, the smearing value of 0.1 eV was used to calculate the adsorption energy of CO on the $Pd_2/TiO_{2\text{-}V}$ catalyst, as shown in Table 1. The result shows that little energy difference exists by using smearing of 0.1 and 0.2 eV, and the structures with different smearing are similar. Furthermore, the smearing value of 0.01 eV with the force convergence set to 0.01 eV $Å^{-1}$ and energy convergence set to 1×10^{-6} eV was employed to calculate the above adsorption energy. This did not affect the adsorption energy by more than 0.1 kJ mol^{-1} as compared to that with the smearing value of 0.2 eV, and the distance between two Pd atoms by more than 0.007 Å. In addition, the Gaussian smearing method with SIGMA = 0.2 eV was also used in previous work.[54,55] Force convergence to 0.03 eV $Å^{-1}$ was used to study the Co-doped TiO_2 structure,[56] as well as CO adsorption and methanation.[57] And energy convergence to 1×10^{-5} eV was employed in investigating the adsorption of CO on Pt/graphene and the oxidation reaction.[58] In this work, the ISPIN value of 2 was set in the INCAR file, and

Table 1 Adsorption energies of CO on $Pd_2/TiO_{2\text{-}V}$ with different smearing values, as well as the corresponding structures

Smearing	0.2 eV	0.1 eV	0.01 eV
E_{ads} (kJ mol^{-1})	−225.4	−226.0	−225.3
$Pd_2/TiO_{2\text{-}V}$	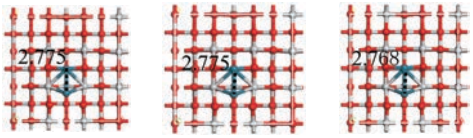		
CO on $Pd_2/TiO_{2\text{-}V}$	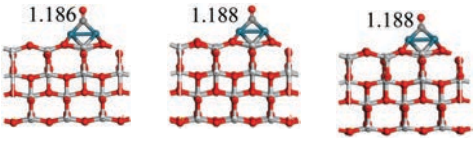		

spin-polarized calculations were performed. However, spin state was not fixed.

The transition state (TS) search was first carried out by the climbing-image nudged elastic band (CI-NEB) method, and then the dimer method was used to optimize the possible image to locate the transition state until the maximum forces on all of the adsorbate atoms as well as the relaxed atoms on the catalysts were converged to less than 0.05 eV Å^{-1}.

The structural stability of $Pd_n/TiO_{2\text{-}V}$ (n = 1, 2, 3, 4 and 6) is expressed by the binding energy (E_b), which is calculated according to eqn (1):

$$E_b = E_{Pd_n} + E_{TiO_{2\text{-}V}} - E_{Pd_n/TiO_{2\text{-}V}} \quad (1)$$

where E_{Pd_n}, $E_{TiO_{2\text{-}V}}$ and $E_{Pd_n/TiO_{2\text{-}V}}$ are the total energies of the Pd clusters, $TiO_{2\text{-}V}$ support and $Pd_n/TiO_{2\text{-}V}$ (n = 1, 2, 3, 4 and 6), respectively.

The adsorption energies (E_{ads}) of the reactants, intermediates and products on $Pd_n/TiO_{2\text{-}V}$ (n = 1, 2, 3, 4 and 6) are calculated using eqn (2):

$$E_{ads} = E_{total} - E_{adsorption\text{-}species} - E_{Pd_n/TiO_{2\text{-}V}} \quad (2)$$

where E_{total}, $E_{adsorption\text{-}species}$ and $E_{Pd_n/TiO_{2\text{-}V}}$ are the electronic energies of the whole adsorbed systems, isolated adsorption species and $Pd_n/TiO_{2\text{-}V}$ (n = 1, 2, 3, 4 and 6), respectively.

The activation energy barrier and reaction energy for every elemental step are calculated, as follows:

$$E_a = E_{TS} - E_{IS} \quad (3)$$

$$E_r = E_P - E_R \quad (4)$$

where E_{TS}, E_R and E_P are the total energies of the transition states, the reactant and the product. The smaller the activation energy barrier, the more favorable the whole process will be.

Calculation models

In this study, the TiO_2(001) surface with an O-vacancy was modeled by a (3 × 3) slab with 12 atomic layers including 4 O–Ti–O repeat units, and the vacuum spacing was set as 15 Å.[41] In the calculation, the bottom 2 O–Ti–O layers were fixed, and the top 2 repeat units and the adsorbed species, including Pd_n clusters and reaction species, were relaxed. The stable isolated Pd_n (n = 1, 2, 3, 4 and 6) clusters were selected by previous studies,[59–61] which are displayed in Fig. 1. And average bond lengths of Pd–Pd were also calculated, and were in line with the previous research work.[62–64] The most stable configuration of $Pd_n/TiO_{2\text{-}V}$ (n = 1, 2, 3, 4 and 6) with 4 O–Ti–O repeat units of $TiO_{2\text{-}V}$ and the corresponding binding energies between Pd_n clusters and $TiO_{2\text{-}V}$ are displayed in Fig. 2.

Results and discussion

Stability of $Pd_n/TiO_{2\text{-}V}$

The electronic structure analysis is studied to explore the relationship between the Pd clusters and $TiO_{2\text{-}V}$ support, and partial density of states (pDOS) of deposited Pd clusters and free Pd clusters are presented in Fig. 3. The shape of the pDOS of supported Pd clusters is changed compared to the gas phase Pd clusters, and is broadened significantly. Meanwhile, the peak height of occupied states below the Fermi level decreases, indicating that an interaction occurs between the Pd clusters and support, which is in agreement with the research by Jia *et al.*,[59] in which Pd_n clusters were supported on graphene with a single vacancy. Moreover, spin states of the singlet and triplet were chosen to calculate the pDOS of $Pd_4/TiO_{2\text{-}V}$, which are shown in Fig. S1 in the ESI.† This also shows that the shape of Pd_4 is broadened after adsorbing on $TiO_{2\text{-}V}$, implying that there is an interaction between Pd_4 and $TiO_{2\text{-}V}$. In addition, the

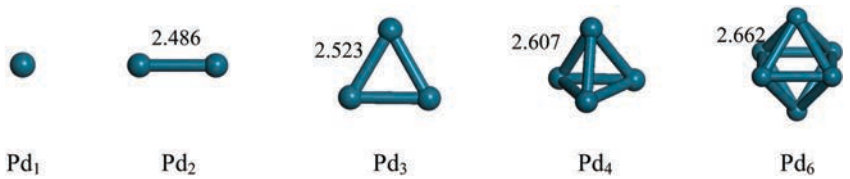

Fig. 1 Most stable configurations of Pd_n (n = 1, 2, 3, 4, 6) clusters and the average bonds of Pd–Pd.

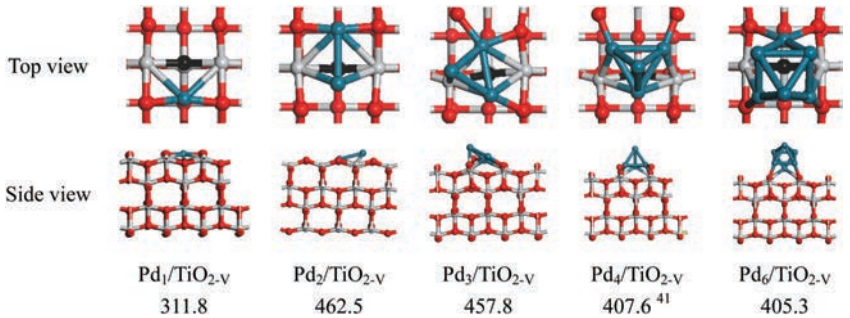

Fig. 2 Top and side views of the most stable configurations of $Pd_n/TiO_{2\text{-}V}$ (n = 1, 2, 3, 4 and 6) and the corresponding binding energies between Pd_n clusters and $TiO_{2\text{-}V}$ (kJ mol^{-1}).

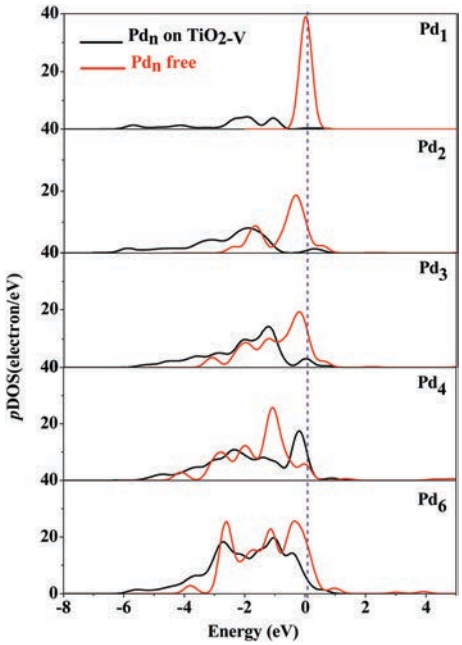

Fig. 3 Partial density of states (pDOS) for Pd_n clusters on $TiO_{2\text{-}V}$ and free Pd_n clusters. The blue dotted line, black line and red line represent the Fermi level, and pDOS of supported Pd clusters and free Pd clusters, respectively.

binding energies between small Pd clusters and $TiO_{2\text{-}V}$ for five catalysts are calculated, which are 311.8, 462.5, 457.8, 407.6 and 405.3 kJ mol^{-1}, respectively. Obviously, Pd_n clusters (n = 1, 2, 3, 4 and 6) have strong binding ability with $TiO_{2\text{-}V}$, implying that there are stable supported catalysts. Previous experiments also proved that small Pd_n clusters can deposit on the metal oxide support stably.[31]

Reaction mechanism for CO catalytic coupling to DMO

We first show the possible mechanism in the process of DMO formation before investigating the effect of Pd clusters with different structures on the reaction. According to previous studies,[5,65] it is found that there are three mechanisms for DMO formation. The difference between the three paths lies in different C–C coupling routes, which is the key step for the conversion of inorganic C1 to organic C2,[66–68] and the detailed content is visible in Fig. 4. The blue line is Path 1 ($COOCH_3$–$COOCH_3$ route), the red line is named as Path 2 (CO–$COOCH_3$ route), and the green line is called Path 3 (CO–CO route).

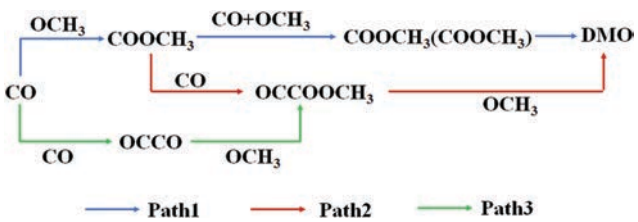

Fig. 4 Different coupling paths of DMO formation by the CO catalytic coupling reaction.[5,65]

CO and OCH_3 co-adsorption on $Pd_1/TiO_{2\text{-}V}$

It is widely reported that single-atom catalysts can maximize the utilization efficiency of metals due to uniform dispersion of single-atoms on the supports.[69] Therefore, we first consider the Pd atom on the $TiO_{2\text{-}V}$ support. The CO catalytic coupling reaction begins with CO and OCH_3 co-adsorbed on $Pd_1/TiO_{2\text{-}V}$, which is attributed to the easy dissociation of CH_3ONO leading to CH_3O and NO on the Pd-based catalysts.[5,67,70] The different co-adsorption configurations of CO and OCH_3 are considered. Unfortunately, CO is easily bound to the O atom on the surface of TiO_2–O_V to form CO_2 after structural optimization, as seen in Fig. 5. Therefore, we conjecture that the structure is unsuitable for the CO catalytic coupling reaction and we do not consider the subsequent reaction on this catalyst. Moreover, the same results were also observed on the surface of CeO_2(111), when Mn or Fe atoms were doped into the surface of CeO_2(111), and the surface O atoms were activated, which made the adsorbed CO on the surface easy to convert to CO_2.[71,72]

CO catalytic coupling reaction on $Pd_2/TiO_{2\text{-}V}$

Every possible reaction pathway for CO catalytic coupling to DMO on the $Pd_2/TiO_{2\text{-}V}$ catalyst is considered, and the OCCO intermediate has not been obtained on the $Pd_2/TiO_{2\text{-}V}$ catalyst. The reaction barrier and the reaction energy of each elementary step in two paths are shown in Table 2, and all of the structures including the initial, intermediate and final states, as well as transition states are displayed in Fig. 6. The potential energy profile for CO catalytic coupling to DMO on the $Pd_2/TiO_{2\text{-}V}$ can be seen in Fig. S2 (ESI†), and the corresponding adsorption energies of stable species are also shown in Table S1 in the ESI.† For the first step CH_3O + CO → $COOCH_3$, the activation energy barrier is 79.0 kJ mol^{-1}. It can be seen from Fig. 6 that intermediate $COOCH_3$ is absorbed at the interface between Pd_2 and $TiO_{2\text{-}V}$. And then, another intermediate $COOCH_3$ is produced *via* TS1-2 in Path 1, which is also adsorbed at the interface, and it needs to overcome an activation energy barrier of 58.6 kJ mol^{-1} in this step. Two $COOCH_3$ *via* TS1-3 couple to form the product of DMO, which is a rate-determining step with a high activation energy of 202.8 kJ mol^{-1}. In Path 2, the stable intermediate $COOCH_3$ is generated, which is attacked by CO to produce intermediate $OCCOOCH_3$ *via* TS1-4. This step requires an activation energy of 73.7 kJ mol^{-1}. Finally, DMO is generated by $OCCOOCH_3$ and OCH_3 adsorbed at the interface *via* TS1-5 with an activation energy of 147.9 kJ mol^{-1}, which has the highest active energy in Path 2. Compared with our pervious study on the $Pd_4/TiO_{2\text{-}V}$ catalyst, the active energy barrier for

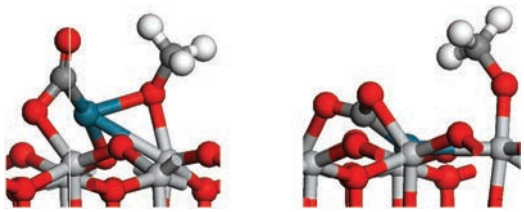

Fig. 5 Optimized structures for the co-adsorption of CO and OCH_3 on $Pd_1/TiO_{2\text{-}V}$.

Table 2 Activation energy (E_a/kJ mol^{-1}) and the reaction energy (E_r/kJ mol^{-1}) for each elementary step during DMO formation on $Pd_2/TiO_{2\text{-}V}$ and $Pd_3/TiO_{2\text{-}V}$ catalysts

Elementary reaction	E_a	E_r	E_a	E_r
	$Pd_2/TiO_{2\text{-}V}$		$Pd_3/TiO_{2\text{-}V}$	
$CO + OCH_3 \rightarrow COOCH_3$	79.0	−44.7	90.3	24.7
$COOCH_3 + CO + OCH_3 \rightarrow COOCH_3 + COOCH_3$	58.6	−86.5	107.4	46.0
$COOCH_3 + COOCH_3 \rightarrow DMO$	202.8	149.8	207.2	98.4
$COOCH_3 + CO \rightarrow OCCOOCH_3$	73.7	37.2	160.1	141.3
$OCCOOCH_3 + OCH_3 \rightarrow DMO$	147.9	84.0	13.3	−69.6

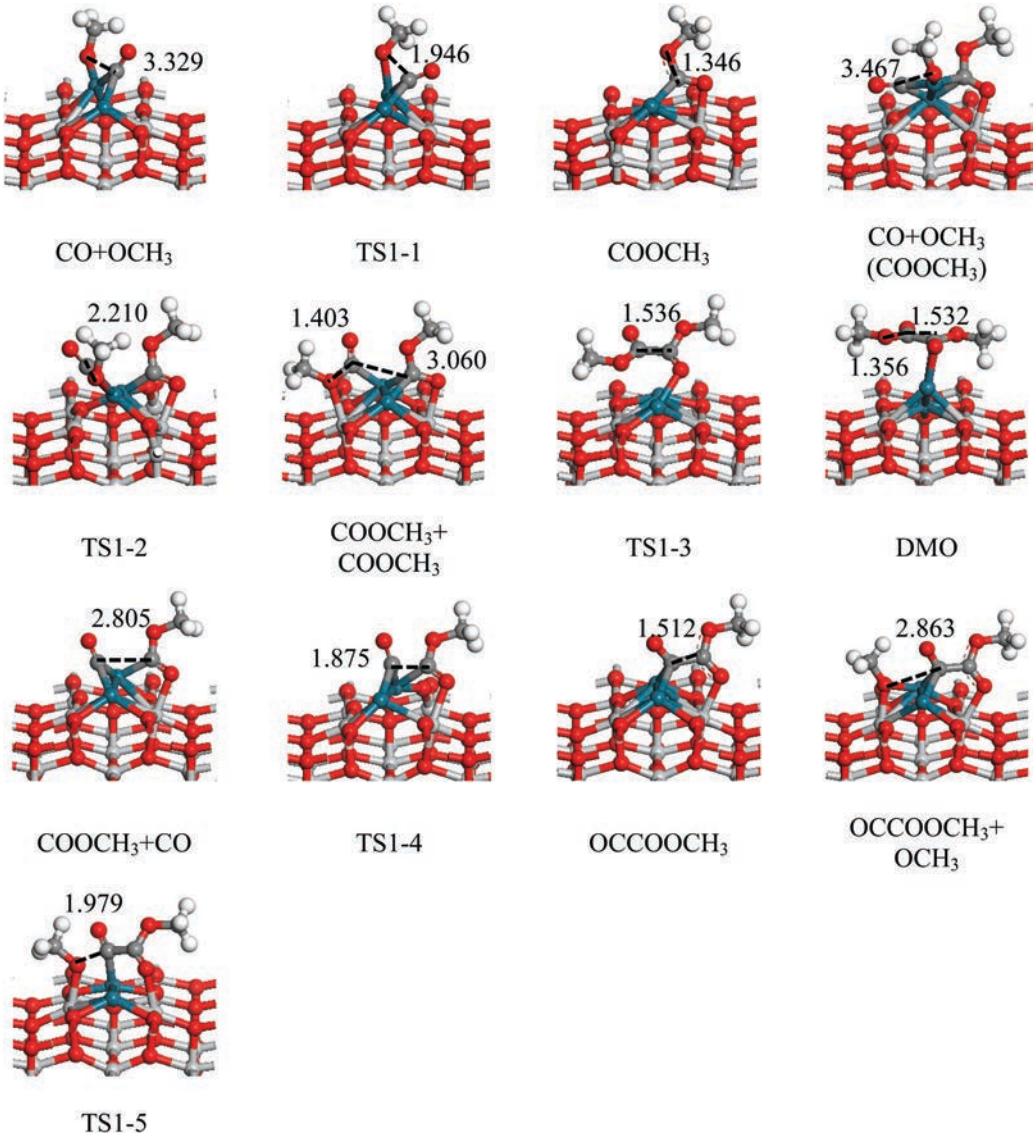

Fig. 6 Configurations of initial, intermediate and final states, as well as transition states for CO catalytic coupling to DMO on $Pd_2/TiO_{2\text{-}V}$.

DMO formation is greatly increased on $Pd_2/TiO_{2\text{-}V}$ (77.0 *vs.* 147.9 kJ mol^{-1}).[41] It is even higher than that on Pd(111), in which an energy barrier of 120.6 kJ mol^{-1} needs to be overcome.[65]

DMO generation on $Pd_3/TiO_{2\text{-}V}$

The reaction path on $Pd_3/TiO_{2\text{-}V}$ is the same as that on the $Pd_2/TiO_{2\text{-}V}$ catalyst, and the potential energy profile and the corresponding adsorption energies of stable species on the $Pd_3/TiO_{2\text{-}V}$ catalyst are shown in Fig. S3 and Table S1 in the ESI.† The reaction also starts with the co-adsorption of CO at the Pd–Pd bridge site and CH_3O at Ti top in $TiO_{2\text{-}V}$ on the $Pd_3/TiO_{2\text{-}V}$ catalyst, to form the first $COOCH_3$ adsorbed at the interface between Pd_3 and $TiO_{2\text{-}V}$ *via* TS2-1 (Fig. 7). There is an activation energy of 90.3 kJ mol^{-1} (see Table 2) in this step,

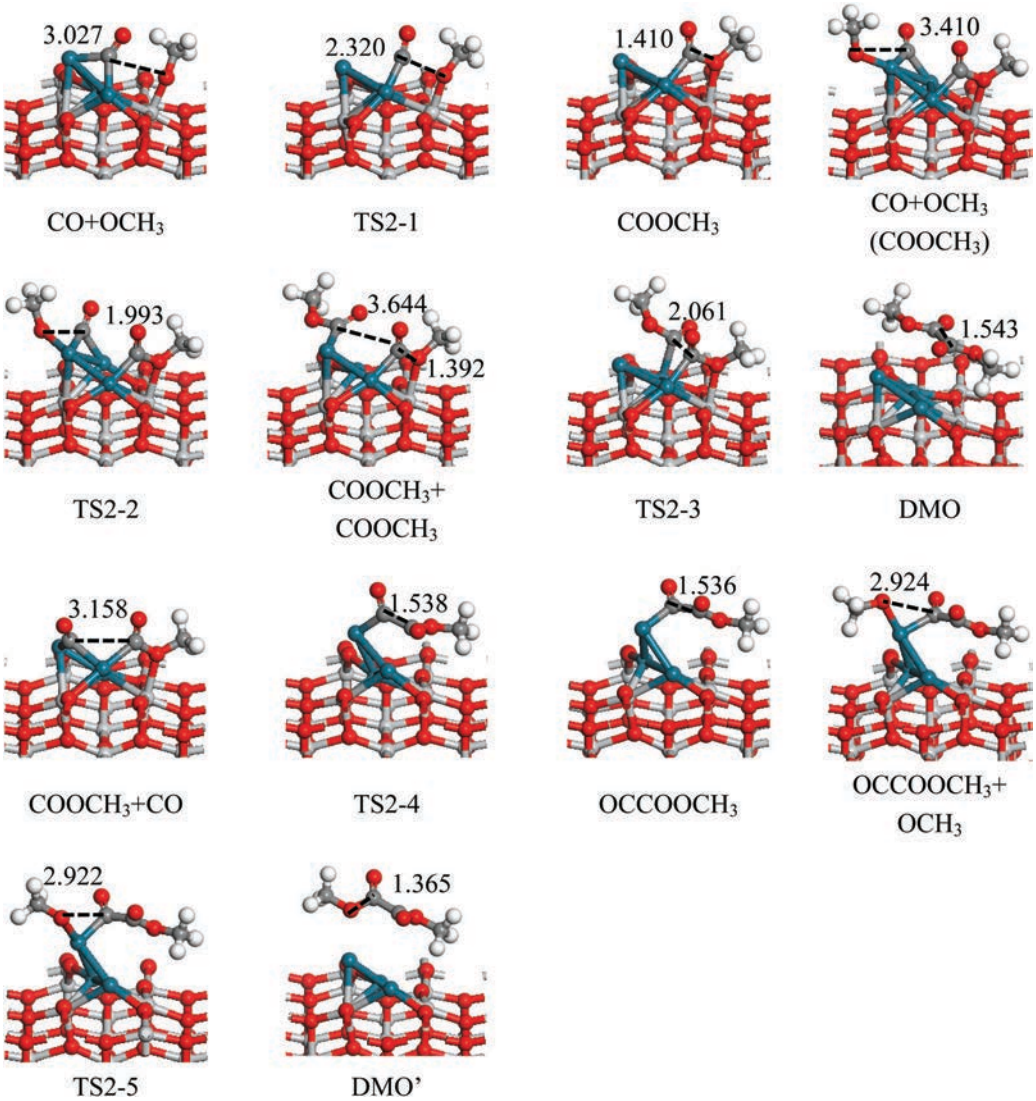

Fig. 7 Configuration of initial states, intermediates and final states, as well as transition states about the CO catalytic coupling reaction to DMO on $Pd_3/TiO_{2\text{-}V}$.

which is a little higher than that on $Pd_2/TiO_{2\text{-}V}$. The second $COOCH_3$ arises *via* TS2-2 by another CO and OCH_3 in the $COOCH_3$–$COOCH_3$ coupling path, which gets over an energy barrier of 107.4 kJ mol^{-1}. The last step will generate a new C–C bond by two $COOCH_3$ *via* TS2-3 with an activation energy of 207.2 kJ mol^{-1}; this also means that our target product DMO is difficult to generate *via* Path 1. Another route is the $COOCH_3$ and CO coupling path, when CO attacks $COOCH_3$ *via* TS2-4 to form $OCCOOCH_3$, and a high energy barrier of 160.1 kJ mol^{-1} needs to be overcome. Finally, DMO is generated by overcoming a minimal barrier with 13.3 kJ mol^{-1}. The rate-determining step in Path 2 is $COOCH_3$ and CO coupling to create a new C–C bond.

As can be seen from the above, the energy barrier of the optimal pathway for the CO catalytic coupling reaction to DMO on $Pd_3/TiO_{2\text{-}V}$ is greater than that on the $Pd_2/TiO_{2\text{-}V}$ catalyst, so it is difficult to synthesize DMO on this catalyst.

CO catalytic coupling to DMO on $Pd_4/TiO_{2\text{-}V}$[41]

CO catalytic coupling to DMO on the $Pd_4/TiO_{2\text{-}V}$ catalyst was studied in our previous work, and the corresponding potential energy profile can be seen in Fig. S4 in the ESI.† The optimal path is the $COOCH_3$–$COOCH_3$ coupling path, and the corresponding activation energies for every elementary reaction are 74.9, 77.0, and 66.7 kJ mol^{-1}.

CO catalytic coupling to DMO on $Pd_6/TiO_{2\text{-}V}$

The potential energy diagram of CO catalytic coupling to DMO on $Pd_6/TiO_{2\text{-}V}$ is displayed in Fig. 8, and all of the reactions are carried out on the Pd_6 cluster. Firstly, the distance between CO and OCH_3 adsorbed at two Pd top sites is 5.003 Å, then a stable intermediate $COOCH_3$ on this catalyst is formed, in which the bond length between the C atom and the O atom in CO and OCH_3 decreases to 1.397 Å *via* TS3-1. An activation energy barrier of 76.3 kJ mol^{-1} is needed.

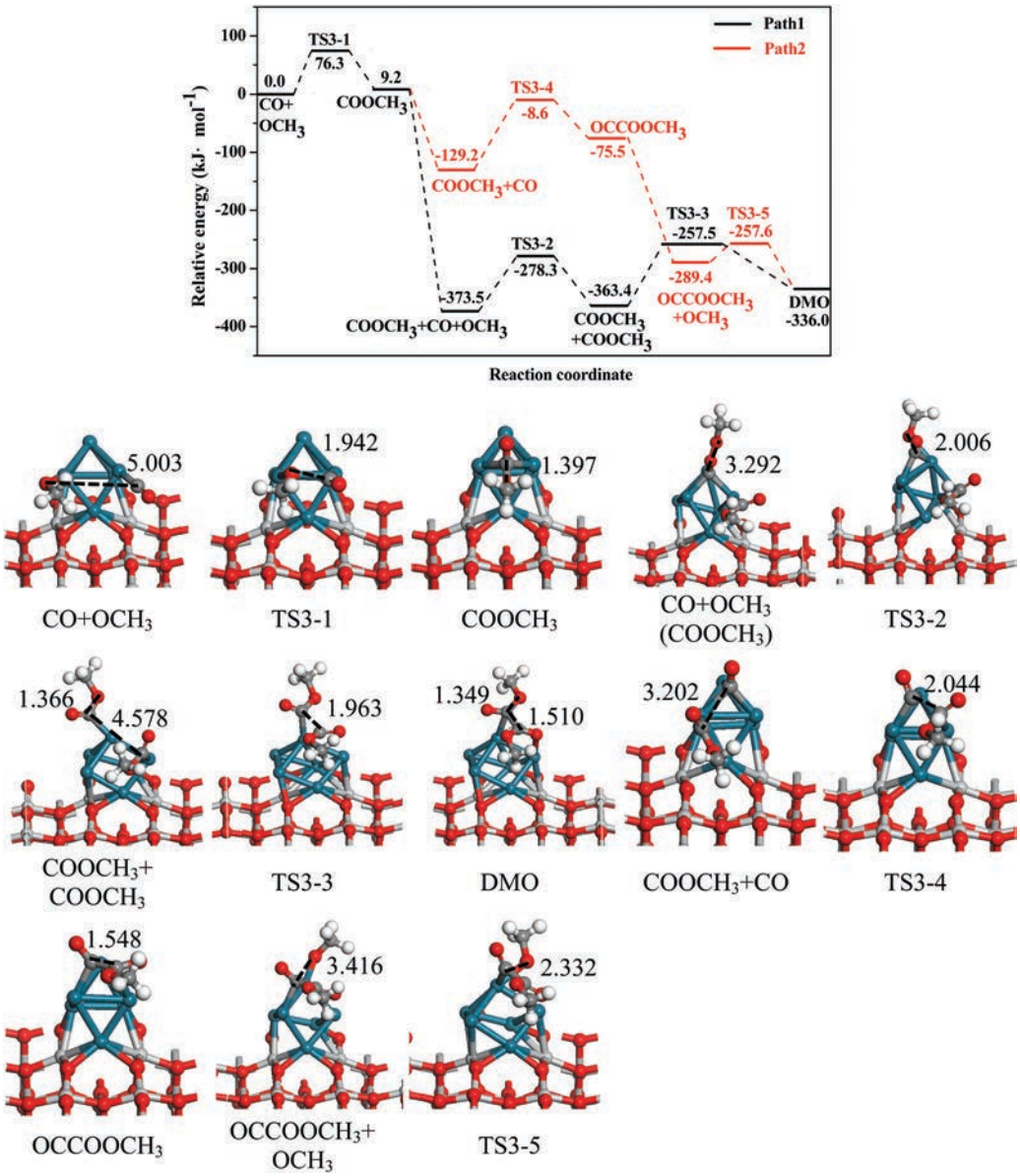

Fig. 8 Potential energy profile for CO catalytic coupling to DMO on the Pd_6/TiO_{2-V} catalyst together with the structures of initial, intermediate and final states, as well as transition states.

In Path 1, when the first $COOCH_3$ is generated at the Pd–Pd bridge site, another $COOCH_3$ is produced through TS3-2 by another CO and OCH_3. In this step, the activation energy is 95.2 kJ mol^{-1}, the distance of C in CO and O in OCH_3 is decreased from 3.292 Å *via* 2.006 Å in TS3-2 and eventually to 1.366 Å. The last elementary reaction in this path is $COOCH_3$ and $COOCH_3$ coupling to DMO *via* TS3-3, this process needs to overcome a higher energy barrier of 105.9 kJ mol^{-1} due to the new C–C bond formed. Thus in Path 1, the step of $COOCH_3$ + $COOCH_3$ → DMO is the rate-determining step.

In Path 2, following the first step for $COOCH_3$ generation, the CO attacks $COOCH_3$ to form a stable intermediate ($OCCOOCH_3$), and this process is also the key step of new bond formation by two C atoms, which overcomes a higher activation energy barrier (120.6 kJ mol^{-1}) than the first step. Subsequently, $OCCOOCH_3$ is attacked by OCH_3, the first C atom in $OCCOOCH_3$ and the O atom in OCH_3 are approached slowly, and their distance changed from 3.416 to 1.349 Å. Eventually, the target product DMO is generated *via* TS3-5, which needs a low energy barrier of 31.8 kJ mol^{-1}.

As mentioned above, on comparing the energy barrier of the two paths (105.9 *vs.* 120.6 kJ mol^{-1}), it is found that the optimal path of CO catalytic coupling to DMO on Pd_6/TiO_2–O_V is the $COOCH_3$–$COOCH_3$ route, which is the same as that on Pd_4/TiO_{2-V}. It can be seen that the activity of Pd_6/TiO_2–O_V is higher than that of Pd(111) and Pd–M (M = Co, Ni, Cu).[65,73] Furthermore, the activity of Pd_6/TiO_2–O_V is also higher than that of Pd_6/SVG.[74]

Selectivity of DMO on different catalysts

In the process of DMO formation, when the first elementary reaction CO + OCH_3 → $COOCH_3$ occurs, by-product dimethyl carbonate (DMC) may be generated by the OCH_3 attacking $COOCH_3$. So the selectivity of DMO is considered relative to DMC.

The active energy barrier of the determining step for DMO and DMC on the four catalysts is displayed in Fig. 9. The activation energy for forming DMO is far greater than that of DMC (69.5 kJ mol^{-1}), which means that there is a poor selectivity to DMO on $Pd_2/TiO_{2\text{-}V}$. As for $Pd_3/TiO_{2\text{-}V}$ and $Pd_4/TiO_{2\text{-}V}$ catalysts, the energy difference between DMO and DMC is 18.9 and 14.0 kJ mol^{-1};[41] this indicates that DMO and DMC are the main products in the CO oxidative coupling process. Concerning the $Pd_6/TiO_{2\text{-}V}$ catalyst, the formation of DMC is extremely difficult with the higher energy barrier than that of DMO, which means that the $Pd_6/TiO_{2\text{-}V}$ catalyst displays an excellent selectivity toward DMO.

Effect of different Pd cluster size on CO catalytic coupling to DMO

For the purpose of investigating the influence of Pd clusters on the adsorption of CO, the relationship between Pd cluster size and CO adsorption energy on $Pd_2/TiO_{2\text{-}V}$, $Pd_3/TiO_{2\text{-}V}$, $Pd_4/TiO_{2\text{-}V}$ and $Pd_6/TiO_{2\text{-}V}$ catalysts is analyzed. CO is adsorbed at different sites of different catalysts to participate in the reaction, and the adsorption structure and the corresponding adsorption energies of CO on $Pd_n/TiO_{2\text{-}V}$ are shown in Table 3. CO is at the Pd–Pd bridge site and the corresponding adsorption energies are −225.4 and −220.9 kJ mol^{-1} on the $Pd_2/TiO_{2\text{-}V}$ and $Pd_3/TiO_{2\text{-}V}$ catalysts, respectively. CO at the bridge site takes part in the reaction, and the adsorption energy is

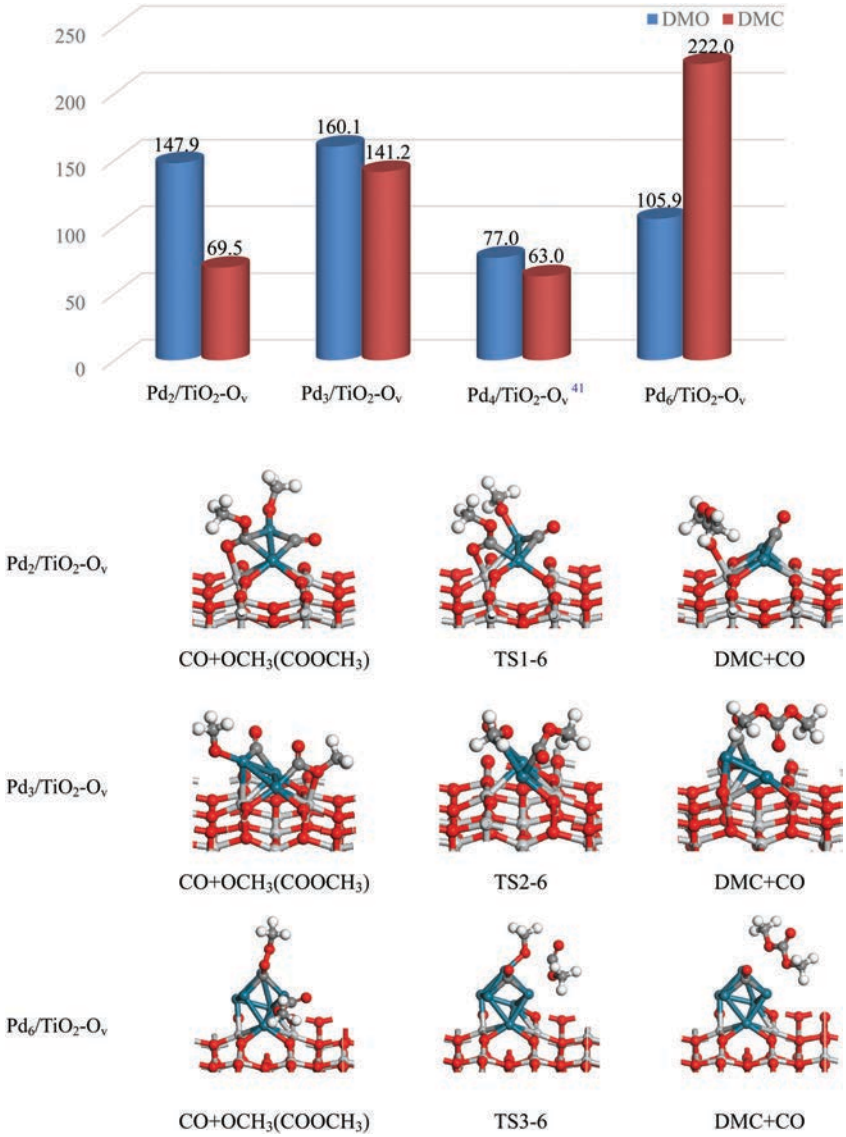

Fig. 9 Activation energy barrier of DMO and DMC on $Pd_2/TiO_{2\text{-}V}$, $Pd_3/TiO_{2\text{-}V}$, $Pd_4/TiO_{2\text{-}V}$ and $Pd_6/TiO_{2\text{-}V}$ catalysts and the corresponding structures of initial states, transition states and final states.

Table 3 Corresponding adsorption energy (kJ mol^{-1}) and the adsorption structure of CO on the $Pd_2/TiO_{2\text{-}V}$, $Pd_3/TiO_{2\text{-}V}$, $Pd_4/TiO_{2\text{-}V}$ and $Pd_6/TiO_{2\text{-}V}$

	$Pd_2/TiO_{2\text{-}V}$	$Pd_3/TiO_{2\text{-}V}$	$Pd_4/TiO_{2\text{-}V}$	$Pd_6/TiO_{2\text{-}V}$
E_{ads}–CO (kJ mol^{-1})	−225.4	−220.9	−144.8	−164.5
Structures	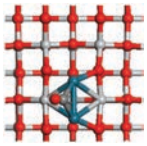	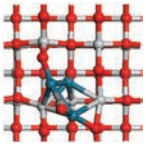	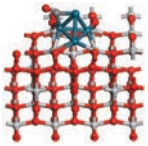	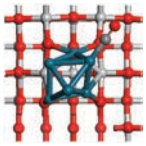

−144.8 kJ mol^{-1} on the $Pd_4/TiO_{2\text{-}V}$ catalyst. Unlike the above three catalysts, CO at the top site participates in the formation of $COOCH_3$ on $Pd_6/TiO_{2\text{-}V}$ and the corresponding adsorption energy is −164.5 kJ mol^{-1}. It can be seen that $Pd_4/TiO_{2\text{-}V}$ and $Pd_6/TiO_{2\text{-}V}$ catalysts show lower adsorption energies of CO as compared to $Pd_2/TiO_{2\text{-}V}$ and $Pd_3/TiO_{2\text{-}V}$ catalysts, which means that CO easily migrates on the surface of $Pd_4/TiO_{2\text{-}V}$ and $Pd_6/TiO_{2\text{-}V}$, and may lead to higher activity, as shown in Fig. 10. In addition, the Bader charge has also been calculated. This shows that charges of 0.23 and 0.17 *e* transfer from the $Pd_2/TiO_{2\text{-}V}$ and $Pd_3/TiO_{2\text{-}V}$ catalysts to CO, respectively. And charges of 0.13 and 0.14 *e* transfer from the $Pd_4/TiO_{2\text{-}V}$ and $Pd_6/TiO_{2\text{-}V}$ catalysts to CO, which shows less charge transfer than that on $Pd_2/TiO_{2\text{-}V}$ and $Pd_3/TiO_{2\text{-}V}$, corresponding to lower adsorption energy of CO. This indicates that the adsorption energy of CO is proportional to the amount of charge transfer. Therefore we can conclude that $Pd_4/TiO_{2\text{-}V}$ and $Pd_6/TiO_{2\text{-}V}$ catalysts exhibit less charge transfer to CO, resulting in weaker adsorption of CO, ultimately leading to higher activity for DMO formation than $Pd_2/TiO_{2\text{-}V}$ and $Pd_3/TiO_{2\text{-}V}$ catalysts.

The optimal reaction paths for the formation of DMO on different catalysts are various. Both CO–$COOCH_3$ and $COOCH_3$–$COOCH_3$ coupling paths aiming at the reaction of DMO formation on $Pd_n/TiO_{2\text{-}V}$ (n = 1, 2, 3, 4 and 6) catalysts have been studied. However, DMO cannot be formed on the $Pd_1/TiO_{2\text{-}V}$ catalyst since CO is easy to react with the O atom on the surface of $TiO_{2\text{-}V}$.

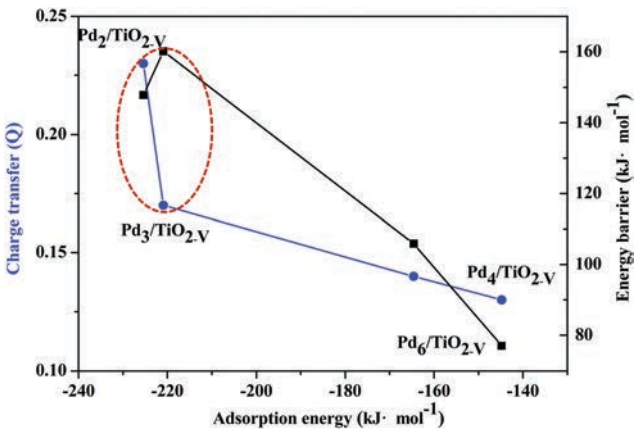

Fig. 10 Relationship between adsorption energy (kJ mol^{-1}) of CO and the charge transfer (*Q*) from $Pd_n/TiO_{2\text{-}V}$ catalysts to CO, as well as the activation energy barrier (kJ mol^{-1}) of the rate-determining step for DMO formation on $Pd_2/TiO_{2\text{-}V}$, $Pd_3/TiO_{2\text{-}V}$, $Pd_4/TiO_{2\text{-}V}$ and $Pd_6/TiO_{2\text{-}V}$ catalysts.

The most optimal paths on $Pd_2/TiO_{2\text{-}V}$ and $Pd_3/TiO_{2\text{-}V}$ are CO–$COOCH_3$ coupling paths, while the rate-limiting steps on the two catalysts are different, which are $OCCOOCH_3 + OCH_3 \rightarrow$ DMO and $COOCH_3 + CO \rightarrow OCCOOCH_3$, and the corresponding activation energy barriers are 147.9 and 160.1 kJ mol^{-1}, respectively. Both on $Pd_4/TiO_{2\text{-}V}$ and $Pd_6/TiO_{2\text{-}V}$ catalysts, the best routes are $COOCH_3$–$COOCH_3$ coupling paths, and the barriers of the rate-determining steps are 77.0 and 105.9 kJ mol^{-1}, as compared to $Pd_2/TiO_{2\text{-}V}$ and $Pd_3/TiO_{2\text{-}V}$ catalysts, which have lower values than the activation barriers and even lower than that on Pd(111).[65] It can be found that the advantageous reaction paths are changed when $n \geq 4$ in the Pd_n cluster, and this is similar to the study by Li *et al.*,[64] in which the favorable reaction pathways for the hydrogenation of acetylene to ethane are different with the change of *n* value. The ethane was formed *via* intermediates of the ethenyl [Pd_n(H)···CH═CH_2] and ethylene [Pd_n···CH_2–CH_2] in Pd_n (n = 2, 3 and 4) clusters, while the other pathway including intermediates of the ethenylidene [Pd_n···CH═CH_2], ethylidyne [Pd_n(H)···C–CH_3] and ethylidene [Pd_n(H)···CH–CH_3] is favorable over Pd_n (n = 5, 6, 7 and 8) clusters.

The order of activity for CO catalytic coupling to DMO on four catalysts abides by the following order: $Pd_4/TiO_{2\text{-}V}$ > $Pd_6/TiO_{2\text{-}V}$ > $Pd_2/TiO_{2\text{-}V}$ > $Pd_3/TiO_{2\text{-}V}$. Obviously, $Pd_4/TiO_{2\text{-}V}$ and $Pd_6/TiO_{2\text{-}V}$ show higher catalytic activity than $Pd_2/TiO_{2\text{-}V}$ and $Pd_3/TiO_{2\text{-}V}$. Furthermore, the reaction active sites are analyzed on these four catalysts. We found that the reaction mainly concentrates on the Pd clusters over $Pd_4/TiO_{2\text{-}V}$ and $Pd_6/TiO_{2\text{-}V}$ with better catalytic activity, while part of the reaction process occurs at the interface between the Pd cluster and $TiO_{2\text{-}V}$ on $Pd_2/TiO_{2\text{-}V}$ and $Pd_3/TiO_{2\text{-}V}$. It is further proved that Pd is the active center for DMO synthesis. Besides, there is a good correlation between electron transfer, CO adsorption and catalytic activity. We can see that the adsorptions of CO on $Pd_4/TiO_{2\text{-}V}$ and $Pd_6/TiO_{2\text{-}V}$ catalysts are weaker than those on $Pd_2/TiO_{2\text{-}V}$ and $Pd_3/TiO_{2\text{-}V}$ catalysts, so CO migrates more easily on these two catalysts and reacts more easily with other species. Therefore, lower activation energies are needed on $Pd_4/TiO_{2\text{-}V}$ and $Pd_6/TiO_{2\text{-}V}$, which exhibit higher activity as compared to $Pd_2/TiO_{2\text{-}V}$ and $Pd_3/TiO_{2\text{-}V}$ catalysts.

Moreover, previous studies also provided that the activity is non-monotonically dependent on deposited cluster size.[31] For DMO synthesis on $Pd_n/TiO_{2\text{-}V}$ (n = 1, 2, 3, 4 and 6), when the load is the Pd_4 cluster, its activity is the highest, followed by the Pd_6 cluster. In addition, spin multiplicity of the singlet and triplet is considered to calculate the energy profile for the rate-determining step ($COOCH_3 + CO + OCH_3 \rightarrow COOCH_3 + COOCH_3$)

Table 4 Structures with average bond lengths (Å) of Pd_4, and relative energies (kJ mol^{-1}) of pure Pd_4 clusters and $Pd_4/TiO_{2\text{-}V}$ with different spin states

	Pd_4	$Pd_4/TiO_{2\text{-}V}$
Spin-singlet state	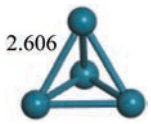 18.4	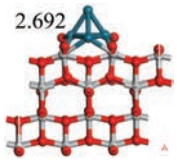 0.0
Spin-triplet state	 0.0	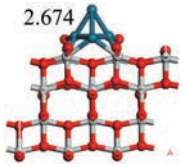 30.3

on $Pd_4/TiO_{2\text{-}V}$ (Fig. S5, ESI†), and the reason for the high activity will be explored. The result shows that the reactant of this rate-determining step favors the spin-singlet state, as well as $Pd_4/TiO_{2\text{-}V}$, which is different from the fact that pure Pd_4 in the spin-triplet state is more stable than the spin-singlet state.[75] The structures and relative energies of pure Pd_4 clusters and $Pd_4/TiO_{2\text{-}V}$ with spin states of singlet and triplet are shown in Table 4. The same result obtained by Zhang *et al.*[76] also showed that the relative energy order of the Pd cluster on TiO_2(110) with spin multiplicity of the singlet and triplet may interchange as compared to the gas phase results. Moreover, the spin-triplet of $Pd_4/TiO_{2\text{-}V}$ is an unstable state, and it contributes to the high activity of $Pd_4/TiO_{2\text{-}V}$, which facilitates the CO oxidative coupling reaction. However, we have to admit that Kohn–Sham density functional theory (KS-DFT) calculation within the projector augmented wave (PAW) method includes spin contamination errors, which affects the energy,[77–81] and further influences the analysis of spin conversion. In addition, clusters with 4 atoms also exhibited high catalytic activity in previous work.[9,82] The Cu_4 cluster supported on Al_2O_3 showed high activity for the conversion of CO_2 to CH_3OH with a low activation barrier *via* X-ray adsorption spectroscopy and DFT calculations. This may also be attributed to its special magic number structure. When studying the removal of Hg^0 on Pd_n/g-C_3N_4, the Pd_4/g-C_3N_4 catalyst enhanced the adsorption of Hg^0, and had better application prospects due to its more active sites than $Pd_{n(n=1\text{–}3)}$/g-C_3N_4.[83] Moreover, the activation energy barriers of DMO formation on Pd_4 and Pd_6 clusters supported on $TiO_{2\text{-}V}$ were 77.0 and 105.9 kJ mol^{-1}, which were lower than that on SVG with 114.5 and 216.3 kJ mol^{-1}.[74]

The formation of DMO and DMC shows that the DMO selectivity on different Pd_n clusters varies greatly. DMC is easily formed on the $Pd_2/TiO_{2\text{-}V}$ catalyst and shows poor DMO selectivity. Both the $Pd_3/TiO_{2\text{-}V}$ and $Pd_4/TiO_{2\text{-}V}$ catalysts exhibit low DMO selectivity, because the activation barrier difference between DMO and DMC is very small, so both DMO and DMC are the main products on these two catalysts. It can also be seen that $Pd_4/TiO_{2\text{-}V}$ exhibits high activity to DMO, but has a poor selectivity. However, $Pd_6/TiO_{2\text{-}V}$ not only shows better catalytic activity than Pd(111), but also has a high selectivity to DMO. Therefore, $Pd_6/TiO_{2\text{-}V}$ is an effective catalyst to improve the activity and selectivity towards DMO generation. In addition, it has been reported that the BN-supported Pd_6 catalyst exhibited a high selectivity to H_2 during the decomposition of HCOOH, and the catalytic activity is higher than that on the Pd(111) surface.[29] In the reaction of cyclohexane oxidation, the graphene oxide supported Ag_6 cluster catalyst exhibited high selectivity to cyclohexanone.[84] The subnanometer-sized $Pd_6(C_{12}H_{25}S)_{11}$ cluster could be synthesized in one-step rapidly under mild conditions, after removing the ligands, and Pd_6 nanoclusters supported on carbon black showed an ultrahigh catalytic activity for the reduction of 4-nitrophenol (4-NP) to 4-aminophenol (4-AP). And the low coordination of Pd atoms in Pd nanoclusters was an important reason for their high catalytic activity.[85] The Pd_6 cluster loaded on single defect graphene as an adsorbent also showed higher selectivity for AsH_3 removal than Pd and Pd_4 clusters.[86] The Pd_6 cluster supported on TiO_2 had also been used to research the reduction of NO by H_2, and the energy barrier for the formation of N_2 on Pd_6/TiO_2 is significantly reduced as compared to that on the Pd(211) surface, implying that Pd_6/TiO_2 exhibits a better selectivity to N_2 than Pd(211).[87,88]

Conclusions

In this work, the DFT method is used to clarify the effect of different small Pd_n (n = 1, 2, 3, 4 and 6) on CO oxidative coupling to DMO. It can be seen that $Pd_1/TiO_{2\text{-}V}$ is not an ideal catalyst for CO oxidation coupling to DMO since the surface of O on TiO_2–O_V is too active to co-adsorb CO and OCH_3. The CO oxidative coupling reaction mainly occurs on the interfaces between the Pd cluster and the $TiO_{2\text{-}V}$ support on $Pd_2/TiO_{2\text{-}V}$ and $Pd_3/TiO_{2\text{-}V}$ catalysts, and the CO–$COOCH_3$ path is favorable. While the $COOCH_3$–$COOCH_3$ path is advantageous on $Pd_4/TiO_{2\text{-}V}$ and $Pd_6/TiO_{2\text{-}V}$, and the reaction occurs on the active component Pd. In addition, the activity of DMO formation on the four catalysts is not linear with the atomic number of the Pd cluster. Pd_4/TiO_2–O_V and Pd_6/TiO_2–O_V exhibit higher activity than Pd_2/TiO_2–O_V and Pd_3/TiO_2–O_V, and also higher activity than that on the Pd(111) surface. The calculation results show that the Pd_6/TiO_2–O_V catalyst exhibits high DMO selectivity compared to the other catalysts. Moreover, $Pd_6/TiO_{2\text{-}V}$ not only has high catalytic activity, but also exhibits high selectivity to DMO, which can be used as a potential catalyst for DMO synthesis.

Conflicts of interest

The authors declare no competing financial interest.

Acknowledgements

We gratefully acknowledge financial support from the Key Projects of National Natural Science Foundation of China

(No. 21736007), the National Natural Science Foundation of China (Grant No. 21576178 and 21476155), the Research Project supported by the Shanxi Scholarship Council of China (No. 2016-030) and the Foundation of State Key Laboratory of Coal Conversion (No. J18-19-602).

References

1 D. M. Fenton and P. J. Steinwan, *J. Org. Chem.*, 1974, **39**, 701–704.
2 T. J. Zhao, D. Chen, Y. C. Dai, W. K. Yuan and A. Holmen, *Ind. Eng. Chem. Res.*, 2004, **43**, 4595–4601.
3 S. Y. Peng, Z. N. Xu, Q. S. Chen, Y. M. Chen, J. Sun, Z. Q. Wang, M. S. Wang and G. C. Guo, *Chem. Commun.*, 2013, **49**, 5718–5720.
4 Z. N. Xu, J. Sun, C. S. Lin, X. M. Jiang, Q. S. Chen, S. Y. Peng, M. S. Wang and G. C. Guo, *ACS. Catal.*, 2012, **3**, 118–122.
5 Q. H. Li, Z. F. Zhou, R. P. Chen, B. Z. Sun, L. Y. Qiao, Y. G. Yao and K. C. Wu, *Phys. Chem. Chem. Phys.*, 2015, **17**, 9126–9134.
6 Y. Ji, G. Liu, W. Li and W. D. Xiao, *J. Mol. Catal. A: Chem.*, 2009, **314**, 63–70.
7 B. Kalita and R. C. Deka, *Bull. Catal. Soc. India*, 2006, **5**, 110–120.
8 G. D. Stein, *Phys. Teach.*, 1979, **17**, 503–512.
9 C. Liu, B. Yang, E. Tyo, S. Seifert, J. DeBartolo, B. von Issendorff, P. Zapol, S. Vajda and L. A. Curtiss, *J. Am. Chem. Soc.*, 2015, **137**, 8676–8679.
10 B. Yang, C. Liu, A. Halder, E. C. Tyo, A. B. F. Martinson, S. Seifert, P. Zapol, L. A. Curtiss and S. Vajda, *J. Phys. Chem. C*, 2017, **121**, 10406–10412.
11 R. Reske, H. Mistry, F. Behafarid, B. Roldan Cueny and P. Strasser, *J. Am. Chem. Soc.*, 2014, **136**, 6978–6986.
12 E. C. Tyo and S. Vajda, *Nat. Nanotechnol.*, 2015, **10**, 577–588.
13 F. S. Roberts, M. D. Kane, E. T. Baxter and S. L. Anderson, *Phys. Chem. Chem. Phys.*, 2014, **16**, 26443–26457.
14 J. Lu, L. Cheng, K. C. Lau, E. Tyo, X. Luo, J. Wen, D. Miller, R. S. Assary, H. H. Wang, P. Redfern, H. Wu, J. B. Park, Y. K. Sun, S. Vajda, K. Amine and L. A. Curtiss, *Nat. Commun.*, 2014, **5**, 4895.
15 S. Proch, M. Wirth, H. S. White and S. L. Anderson, *J. Am. Chem. Soc.*, 2013, **135**, 3073–3086.
16 W. E. Kaden, T. Wu, W. A. Kunkel and S. L. Anderson, *Surf. Sci.*, 2009, **326**, 826–829.
17 D. Sen, R. Thapa and K. K. Chattopadhyay, *Int. J. Hydrogen Energy*, 2013, **38**, 3041–3049.
18 M. Y. Ni and Z. Zeng, *THEOCHEM*, 2009, **910**, 14–19.
19 X. F. Wang and L. Andrews, *J. Phys. Chem. A*, 2001, **105**, 5812–5822.
20 X. Gao and W. Chen, *Chem. Commun.*, 2017, **53**, 9733–9736.
21 P. Tian, D. Ding, Y. Sun, F. Xuan, X. Xu, J. Xu and Y. F. Han, *J. Catal.*, 2019, **369**, 95–104.
22 A. S. Wörz, K. Judai, S. Abbet and U. Heiz, *J. Am. Chem. Soc.*, 2003, **125**, 7964–7970.
23 B. T. Qiao, J. X. Liang, A. Q. Wang, J. Y. Liu and T. Zhang, *Chin. J. Catal.*, 2016, **37**, 1580–1586.
24 T. Abdollahi and D. Farmanzadeh, *Appl. Surf. Sci.*, 2018, **433**, 513–529.
25 M. C. Valero, P. Raybaud and P. Sautet, *J. Catal.*, 2007, **247**, 339–355.
26 I. Stara, V. Nehasil and V. Matolin, *Surf. Sci.*, 1995, **331**, 173–177.
27 S. Tanabe and H. Matsumoto, *J. Mater. Sci. Lett.*, 1994, **13**, 1540–1542.
28 H. Matsumoto and S. Tanabe, *J. Phys. Chem.*, 1995, **99**, 6951–6956.
29 R. Schimmenti, R. Cortese and D. Duca, *ChemCatChem*, 2017, **9**, 1610–1620.
30 W. Xiao, R. Zeng, L. Cheng, J. W. Wang, L. J. Jiang and L. G. Wang, *RSC Adv.*, 2015, **5**, 61861–61867.
31 M. D. Kane, F. S. Roberts and S. L. Anderson, *Faraday Discuss.*, 2013, **162**, 323–340.
32 U. Diebold, *Surf. Sci. Rep.*, 2003, **48**, 53–229.
33 T. Berger, M. Sterrer, O. Diwald, E. Knözinger, D. Panayotov, T. L. Thompson and J. T. Yates, *J. Phys. Chem. B*, 2005, **109**, 6061–6068.
34 M. V. Ganduglia-Pirovano, A. Hofmann and J. Sauer, *Surf. Sci. Rep.*, 2007, **62**, 219–270.
35 Y. Li, B. Xu, Y. Fan, N. Feng, A. Qiu, J. M. J. He, H. Yang and Y. Chen, *J. Mol. Catal. A: Chem.*, 2004, **216**, 107–114.
36 J. Panpranot, K. Kontapakdee and P. Praserthdam, *J. Phys. Chem. B*, 2006, **110**, 8019–8024.
37 H. Yin, Y. Wada, T. Kitamura, S. Kambe, S. Murasawa, H. Mori, T. Sakata and S. Yanagida, *J. Mater. Chem.*, 2001, **11**, 1694–1703.
38 J. Yang, L. X. Cao and G. C. Wang, *J. Mol. Model.*, 2012, **18**, 3329–3339.
39 J. F. Sanz and A. Márquez, *J. Phys. Chem. C*, 2007, **111**, 3949–3955.
40 J. Yang, C. Q. Lv, Y. Guo and G. C. Wang, *J. Chem. Phys.*, 2012, **136**, 104107.
41 Y. T. Cao, L. X. Ling, H. Lin, M. H. Fan, P. Liu, R. G. Zhang and B. J. Wang, *Comput. Mater. Sci.*, 2019, **159**, 1–11.
42 J. Lu, J. Song, H. Niu, L. Pan, X. Zhang, L. Wang and J. J. Zou, *Appl. Surf. Sci.*, 2016, **371**, 61–66.
43 C. H. Sun and S. C. Smith, *J. Phys. Chem. C*, 2012, **116**, 3524–3531.
44 S. W. Liu, J. G. Yu and M. Jaroniec, *Chem. Mater.*, 2011, **23**, 4085–4093.
45 S. Y. Peng, Z. N. Xu, Q. S. Chen, Y. M. Chen, J. Sun, Z. Q. Wang, M. S. Wang and G. C. Guo, *Chem. Commun.*, 2013, **49**, 5718–5720.
46 Y. Yamamoto, T. Matsuzaki, S. Tanaka, K. Nishihira, K. Ohdan, A. Nakamura and Y. Okamoto, *J. Chem. Soc., Faraday Trans.*, 1997, **93**, 3721–3727.
47 V. A. Spasov and K. M. Ervin, *J. Chem. Phys.*, 1998, **109**, 5344–5350.
48 L. X. Ling, L. L. Fan, X. Feng, B. J. Wang and R. G. Zhang, *Chem. Eng. J.*, 2017, **308**, 289–298.
49 H. A. Duarte and D. R. Salahub, *Top. Catal.*, 1999, **9**, 123–133.
50 A. S. Wörz, K. Judai, S. Abbet and U. Heiz, *J. Am. Chem. Soc.*, 2003, **125**, 7964–7970.
51 G. Kresse and J. Furthmüller, *Phys. Rev. B: Condens. Matter Mater. Phys.*, 1996, **54**, 11169–11186.

52 G. Kresse and D. Joubert, *Phys. Rev. B: Condens. Matter Mater. Phys.*, 1999, **59**, 1758–1775.
53 J. P. Perdew, K. Burke and M. Ernzerhof, *Phys. Rev. Lett.*, 1996, **77**, 3865–3868.
54 G. A. Ferguson, V. Vorotnikov, N. Wunder, J. Clark, K. Gruchalla, T. Bartholomew, D. J. Robichaud and G. T. Beckham, *J. Phys. Chem. C*, 2016, **120**, 26249–26258.
55 C. J. Shang, B. Xu, X. L. Lei, S. C. Yu, D. C. Chen, M. S. Wu, B. Z. Sun, G. Liu and C. Y. Ouyang, *Phys. Chem. Chem. Phys.*, 2018, **20**, 20919–20926.
56 W. T. Geng and K. S. Kim, *Solid State Commun.*, 2004, **129**, 741–746.
57 J. X. Liu, H. Yan and W. X. Li, *Catal. Today*, 2013, **215**, 36–42.
58 Y. N. Tang, Z. X. Yang and X. Q. Dai, *Phys. Chem. Chem. Phys.*, 2012, **14**, 16566–16572.
59 T. T. Jia, C. H. Lu, K. N. Ding, Y. F. Zhang and W. K. Chen, *Comput. Theor. Chem.*, 2013, **1020**, 91–99.
60 R. Robles and S. N. Khanna, *Phys. Rev. B: Condens. Matter Mater. Phys.*, 2010, **82**, 085428.
61 Y. Jiang, W. Chu, C. F. Jiang and Y. H. Wang, *Acta Phys.-Chim. Sin.*, 2007, **23**, 1723–1727.
62 G. Zanti and D. Peeters, *Eur. J. Inorg. Chem.*, 2009, 3904–3911.
63 I. Cabria, M. J. López and J. A. Alonso, *Phys. Rev. B: Condens. Matter Mater. Phys.*, 2010, **81**, 035403.
64 J. N. Li, M. Pu, C. C. Ma, Y. Tian, J. He and D. G. Evans, *J. Mol. Catal. A: Chem.*, 2012, **359**, 14–20.
65 B. Y. Han, X. Feng, L. X. Ling, M. H. Fan, P. Liu, R. G. Zhang and B. J. Wang, *Phys. Chem. Chem. Phys.*, 2018, **20**, 7317–7332.
66 J. G. Fang, B. W. Wang, Z. H. Li and G. H. Xu, *React. Kinet. Catal. Lett.*, 2003, **80**, 293–301.
67 C. Fan, M. Luo and W. D. Xiao, *Chin. J. Chem. Eng.*, 2016, **24**, 132–139.
68 F. Meng, G. H. Xu and Q. R. Guo, *J. Mol. Catal. A: Chem.*, 2003, **201**, 283–288.
69 X. F. Yang, A. Q. Wang, B. T. Qiao, J. Liu and T. Zhang, *Acc. Chem. Res.*, 2013, **46**, 1740–1748.
70 C. J. Cassady and B. S. Freiser, *J. Am. Chem. Soc.*, 1985, **107**, 1566–1573.
71 L. C. Hsu, M. K. Tsai, Y. H. Lu and H. T. Chen, *J. Phys. Chem. C*, 2012, **117**(1), 433–441.
72 H. T. Chen and J. G. Chang, *J. Phys. Chem. C*, 2011, **115**, 14745–14753.
73 B. Y. Han, H. Lin, L. X. Ling, P. Liu, M. H. Fan, B. J. Wang and R. G. Zhang, *Appl. Surf. Sci.*, 2019, **465**, 498–508.
74 L. X. Ling, X. Feng, Y. T. Cao, P. Liu, M. H. Fan, R. G. Zhang and B. J. Wang, *Mol. Catal.*, 2018, **453**, 100–112.
75 E. D. German, I. Efremenko and M. Sheintuch, *J. Phys. Chem.*, 2001, **105**, 11312–11326.
76 J. Zhang and A. N. Alexandrova, *J. Chem. Phys.*, 2011, **135**, 174702.
77 K. Yamaguchi, T. Kawakami, Y. Takano, Y. Kitagawa, Y. Yamashita and H. Fujita, *Int. J. Quantum Chem.*, 2002, **90**, 370–385.
78 L. Noodleman, T. Lovell, W. G. Han, J. Li and F. Himo, *Chem. Rev.*, 2004, **104**, 459–508.
79 G. David, F. Wennmohs, F. Neese and N. Ferré, *Inorg. Chem.*, 2018, **57**, 12769–12776.
80 K. Tada, T. Maruyama, H. Koga, M. Okumura and S. Tanaka, *Molecules*, 2019, **24**, 505.
81 K. Tada, S. Tanaka, T. Kawakami, Y. Kitagawa, M. Okumura and K. Yamaguchi, *Appl. Phys. Express*, 2019, **12**, 115506.
82 S. Liu, L. Chen, X. Mu, M. Xu, J. Yu, G. Yang, X. Luo, H. Zhao and T. Wu, *Fuel*, 2019, **254**, 115537.
83 S. Liu, L. Chen, X. Mu, M. Xu, J. Yu, G. Yang, X. Luo, H. Zhao and T. Wu, *Fuel*, 2019, **254**, 115537.
84 R. Anumula, C. Cui, M. Yang, J. Li and Z. Luo, *J. Phys. Chem. C*, 2019, **123**, 21504–21512.
85 Z. Zhuang, Q. Yang and W. Chen, *ACS Sustainable Chem. Eng.*, 2019, 7(3), 2916–2923.
86 M. Kunaseth, T. Mudchimo, S. Namuangruk, N. Kungwan, V. Promarak and S. Jungsuttiwong, *Appl. Surf. Sci.*, 2016, **367**, 552–558.
87 L. X. Ling, Y. T. Cao, Z. B. Zhao, P. Liu, B. J. Wang, R. G. Zhang and D. B. Li, *Comput. Mater. Sci.*, 2018, **149**, 182–190.
88 L. X. Ling, Z. B. Zhao, X. Feng, Q. Wang, B. J. Wang, R. G. Zhang and D. B. Li, *J. Phys. Chem. C*, 2017, **121**, 16399–16414.

